Petroleum Science 18 (2021) 1507–1519

Contents lists available at ScienceDirect

Petroleum Science

journal homepage: www.keaipublishing.com/en/journals/petroleum-science

Original Paper

Internal flow mechanism of cone-straight nozzle

Tian-Wen Jiang, Zhong-Wei Huang*, Jing-Bin Li, Yi-Su Zhou

State Key Laboratory of Petroleum Resources and Prospecting, China University of Petroleum (Beijing), Beijing, 102249, China

ARTICLE INFO

Article history:
Received 9 December 2020
Accepted 29 March 2021
Available online 1 September 2021

Edited by Xiu-Qiu Peng

Keywords:
Cone-straight nozzle
Boundary layer
Flow resistance

ABSTRACT

Cone-straight nozzle has been widely used in well bore cleaning, assisting drilling in petroleum industries due to its good clustering properties. The structure including cone angle and throat length has also been studied by scholars and been optimized. However, the internal flow properties have not been investigated clearly especially the boundary layer flow. In this paper LES model is used to capture the small-scale flow state near the nozzle wall. The RNG k-epsilon model is used to validate the accuracy of the LES simulation, the simulation data shows a good agreement. Three different inlet velocities are considered in simulations. The velocity distribution, shear stress, boundary layer thickness, skin friction coefficient and Reynolds stress are analyzed, the boundary layer separation and transition are discussed. The state of flow inside nozzle is laminar with inlet velocity of 1 m/s and gradually transferred into turbulent with the increasing inlet velocity. The most severe turbulence is at the entrance of the throat section, the vortex structure appears at the entrance of converging section and dose not survive, the vortex structure appears in sequence along the throat section wall when the inlet velocity is set to 5 m/s and 10 m/s the flow properties along the conical nozzle are revealed clearly, the main flow resistance is mainly produced in throat section. All these works aim to provide theoretical support for the further processing optimization of the nozzle structure and reduce the flow resistance of nozzle.

1. Introduction

Water jet technology has been used in industry fields widely such as cleaning, cutting, rock breaking, polishing and spray (Folkes, 2009; Guha et al., 2011; Sou et al., 2007) Water is easy to collect and non-polluted, so the technology is economic and environmentally friendly, due to its cooling effect, the technology is used to cut some special materials which used in aerospace and some other special fields. And in petroleum fields, cone-straight nozzle can be used in assisting rock breaking and wellbore cleaning, the nozzle structure plays an important role in effect. (see Table 1)

Many simulations are done to simulate nitrogen jets with different nozzle structures (Dong, 2016; Shi et al., 2021; Wang et al., 2013). Simulation results show that the cone-straight nozzle has better clustering, the cone-shaped nozzle has better dispersion, and the flat-tube nozzle has the largest running distance. The experiment verifies the cutting ability before and after nozzle optimization. The flow field characteristics and rock-breaking characteristics of cone-straight nozzles and cone-shaped nozzles were compared through experiments and numerical simulations (Ma and Pan, 2019; Tafreshi and Pourdeyhimi, 2003). Aiming at constant jet velocity and length, the simulation results show that cone-shaped nozzles are excellent. Cone nozzles and flat nozzles. The influence of nozzle cone angle on the jet parameters was investigated through numerical simulations, and the jet velocity first increases and then decreases with the increase of the cone angle (Liu and Cheng, 2020). The effect of different nozzles on hydrate breaking, the optimization results were compared through numerical simulation and orthogonal experiment (Chen et al., 2019), and the optimized structure parameters of the cone-straight nozzle are suggested. In addition, in the use of water jet to eliminate residual stress, the cone-straight nozzle has a better application effect, thanks to the function of its straight pipe section with stable jet characteristics. According to the research of scholars, the jetting effect is best when the inclination angle of the contraction section is 13–15° and the length of the throat pipe section is 2–4 times the diameter of the throat.

Water jet technology refers to the use of high-pressure water generating equipment to generate high-pressure water, and the

* Corresponding author.
E-mail address: huangzw@cup.edu.cn (Z.-W. Huang).

https://doi.org/10.1016/j.petsci.2021.08.008

Table 1
Nozzle structure parameters.

Parameter	D_1	D_2	L	α
Value	15 mm	4 mm	12 mm	15°

pressure is converted into a highly concentrated water jet through a nozzle, nozzle is the important part and has been investigated for years.

Nozzle structure is proposed by many scholars for different application. And the flow properties have been investigated. For cleaning, cutting and rock breaking, cone-straight nozzle is the most commonly used, and the structure plays an important role in flow properties, cone-straight nozzle consists of conical section and throat section, the conical section is used to contract the flow bunch, and the throat section is used to steady the flow to gain a longer flow core. The cone angle and length of throat section have been optimized by experiments and simulations. In petroleum fields discharge coefficient and the length of flow core are two main parameters for evaluating nozzle performance. To obtain a higher discharge coefficient and longer flow core length, the internal boundary layers of the nozzle should be investigated and the factors affecting flow resistance need to be revealed clearly. However, many scholars pay more attention to compressive gas flow and the water flow is ignored.

The nozzle exit boundary layer plays an important role in outer flow field, the influence of boundary layer on jet noise and outer turbulent shear layer was discussed (Fontaine et al., 2015), LES simulation was used to investigate the effects of moderate Reynolds numbers on subsonic round jets with highly disturbed nozzle-exit boundary layers, the mixing layers developed more slowly, with smaller integral length scales and lower levels of velocity with Reynolds number increasing (Bogey and Bailly, 2010). And the differences in radiated noise between the initially laminar and turbulent jets are related to the differences in growth rate of the Kelvin–Helmholtz mode in the near-nozzle region fluctuations (Brès et al., 2018). The reason of jet noise increasing was revealed, and the nozzles involving turbulent boundary layers were the quietest while nozzles involving a “nominally laminar” boundary layer were loud especially on the high-frequency side of the sound pressure level spectrum, the dynamics and interaction of these coherent structures lead to higher turbulence as well as higher levels of high-frequency noise (Zaman, 2017). the influence of nozzle structure on jet noise of subsonic nozzle was discussed, and the noisier nozzle involves a highly disturbed laminar, or nominally laminar, boundary-layer state as opposed to a turbulent state with the other, some experiments to investigate the effect of initial condition on subsonic jet noise were done (KBMQ, 1985; Zaman, 2012). A study which looked at the nozzle exit boundary layer as a possible factor for the difference of jet noise was developed, some measurements of different nozzles such as ASME nozzles, conical nozzles were done, the results showed that as the laminar boundary layer transitions to turbulent, the high-frequency jet noise is reduced (Karon and Ahuja, 2017). When gas flows through the nozzle, FDA nozzle and supersonic nozzle were proposed and discussed, the effect of turbulence on transitional flow in FDA's benchmark nozzle was discussed by experiment and large eddy simulations and the results is that the shear peak appeared at the nozzle throat (Manchester and Xu, 2020). Some scholar did many velocity tests by PIV, tested the velocity distribution in three independent laboratories, analyzed the viscous shear stress, velocity distribution, and pressure distribution of the nozzle, aimed to support validation of computational fluid simulations (Hariharan et al., 2011). The transitional and turbulent flow through the FDA benchmark nozzle model using Laser Doppler Velocimetry was analyzed (Taylor et al., 2016). The flow characteristics of pressure oscillation and velocity phase diagrams of different self-excited oscillating modes were analyzed and a full Navier-Stokes viscous laminar model was established for non-equilibrium condensing steam flow (Wang et al., 2018). The shock location inside the divergent section of convergent-divergent nozzle was studied by experiments and a curve-fit equation representing the average trend is provided to predict the throat-to-shock-location distance at a given nozzle pressure ratio (Zaman et al., 2011). Critical-flow venturi nozzle is a popular nozzle to be studied, the critical-flow venturi nozzle discharge coefficient dependency on Reynolds number and wall temperature were investigated by series of two dimensional axisymmetric and adiabatic CFD simulations (Nozzles), and the scholar presented that the wall temperature effect is stronger for small nozzle diameters, also presented that the CFD simulations can predicted the transition of boundary layer of the inner flow. In order to investigate the flow states of critical-flow venturi nozzles (Spotts et al., 2013), extensive numerical investigations were carried put to characterize critical back pressure ratio, instability and boundary layer transition features of critical-flow venturi nozzles, and experiments were also carried out to determine CBPR of five nozzle, the results showed that boundary layer transition mechanism could be captured well with simulations and the comparison with experimental results showed the same tendency, the transitional Reynolds number depends on throat diameter for diameters smaller than around 8 mm and for higher diameter it stays almost constant (Ünsal et al.). The discharge coefficient of a circular-arc critical venturi nozzle was derived theoretically by combining theories to calculate mass flow defects caused by the core flow distribution and the laminar boundary layer, and the equation was verified by measurement using a constant volume tank system and nozzles of similar shaped by super accurate lathes (Ishibashi, 2015; Ishibashi and Takamoto, 2000). And the discharge coefficient function was improved later (Kim et al., 2008), the computational results showed that the critical pressure ratio and the discharge coefficient for ideal gas assumptions are significantly different from those of the real gas, as the Reynolds number exceeds a certain value. A new turbulence models was proposed which had the capability to predict the boundary layer transition of CFVNs, the experimental results showed a good agreement with the simulation results, and found that laminar and turbulent velocity profiles at the throat shows only difference near to the wall and the transitional Re shows diameter dependence for diameters below 10 mm (Ünsal et al., 2016).

There is big difference between compressible fluid and incompressible, the FDA and CFVNs has been investigated by many scholars with gas flowing, while the true water flow performance in the cone-straight nozzle remains unclear. In this paper many simulations are done to reveal the real flow properties of internal flow of the cone-straight nozzle. The location of flow resistance inside cone-straight nozzle will be revealed, and that will give some guidance to reduce the flow resistance inside cone-straight nozzle when it is used in breaking rock in petroleum fields, and that will contribute to the accuracy of the prediction of pump pressure and save energy in drilling and cleaning.

2. Models

2.1. Geometry model

Cone-straight nozzle consists of conical section and throat section, the structure is shown as Fig. 1, D_1 is the inlet diameter, D_2 is the outlet diameter also named throat diameter, L represent the

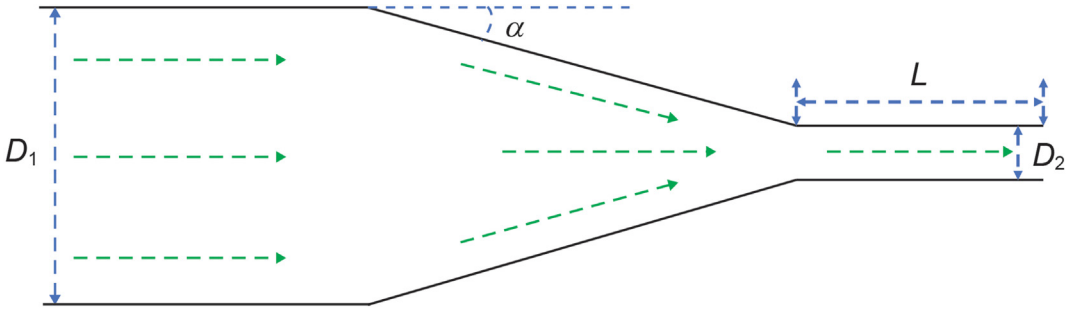

Fig. 1. Structure of cone-straight nozzle.

length of throat section, α represents the half coning angle, the parameters are as follows.

2.2. Grid

Due to the large demand for boundary layer grids, this paper uses the symmetry plane setting for numerical simulation. In order to obtain the real flow state of the near-wall flow, the first layer high must be small enough, in this paper the first layer high is set at $y^+ \approx 1$, and the boundary layer mesh is divided into 20 layers. The grid is shown as Fig. 2.

$$y_p = \frac{y^+ \nu}{U_\tau} \tag{1}$$

$$y^+ = \frac{y_p U_\tau}{\nu} \tag{2}$$

$$U_\tau = \sqrt{\frac{\tau_w}{\rho}} = \sqrt{\frac{\overline{C_f}}{2}} \tag{3}$$

$$\frac{\overline{C_f}}{2} \approx \frac{0.039}{R_{e_{D_h}}^{1/4}} \tag{4}$$

Where y_p is the real height of first grid layer, m, y^+ represents the dimensionless height of first grid layer, ν represents the kinematic viscosity, Pa.s, τ_w is the shear stress, Pa, R_e is the Reynold number, D_h is the hydraulic radius, m. U_τ represents the shear velocity, m/s, and $\overline{C_f}$ represents the average pipe skin friction coefficient.

The structured grid is used for division, and the grid size of the first layer is calculated. The boundary layer is 20 layers and the growth rate is 1.15. After the grid at the near wall is determined, the grid at the non-near wall is further optimized to reduce the calculation amount, and the calculation domain is symmetrically processed. At the same time, the maximum surface size of the middle grid is set to 0.001 m, and the number of grids is reduced from 487540 to 368523. The grid of skewness is 0.68, and the grid quality is good. And the distribution of y^+ along the wall surface is shown as Fig. 3.

2.3. Governing equation

Large eddy simulations have the capacity to capture transitional and turbulence flow and can be utilized to simulate the real performance of initial flow of the cone-straight nozzle, LES numerically resolves the large scales of flow and box filter function is used to filter out the smaller scales, the smaller scales can be resolved by a sub grid-scale model. The spatially filtered Navier-Stokes equations for an incompressible fluid are given by the filtered continuity and momentum equations.

$$\begin{aligned} G(x-\xi) &= \frac{1}{\Delta}\theta\left(\frac{\Delta}{2} - |x-\xi|\right) \\ \theta(\eta) &= 1, \eta > 0 \\ \theta(\eta) &= 0, \eta < 0 \end{aligned} \tag{5}$$

$$\frac{\partial \overline{u_i}}{\partial x_i} = 0 \tag{6}$$

$$\frac{\partial \overline{u_i}}{\partial t} + \frac{\partial}{\partial x_j}\left(\overline{u_i u_j}\right) = -\frac{1}{\rho}\frac{\partial \overline{p}}{\partial x_i} + \nu \frac{\partial}{\partial x_j}\left(\frac{\partial \overline{u_i}}{\partial x_j}\right) - \frac{\partial \tau_{ij}}{\partial x_j} \tag{7}$$

Where u_i is the velocity, the pressure, ρ is the density and ν is the kinematic viscosity. The overbar denotes spatial filtering, accounting for the resolved velocity and pressure fields. The contribution from the small scales are modelled by the sub grid-scale term τ_{ij},

$$\tau_{ij} - \frac{1}{3}\tau_{kk}\delta_{ij} = -2\nu_T \overline{S}_{ij} \tag{8}$$

where S_{ij} is the strain-rate tensor of the resolved field and ν_T represents the modelled eddy-viscosity. In the present study, the wall-adapting local eddy-viscosity (WALE) model is adopted. The WALE model reads

$$\nu_T = (C_w \Delta)^2 D_w(u) \tag{9}$$

where C_w is the constant model coefficient ($C_w = 0.325$), Δ is the filter width which is based on the size of the mesh cells and D_w is an

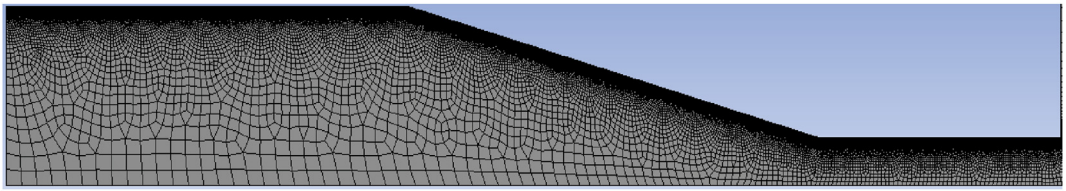

Fig. 2. Grid.

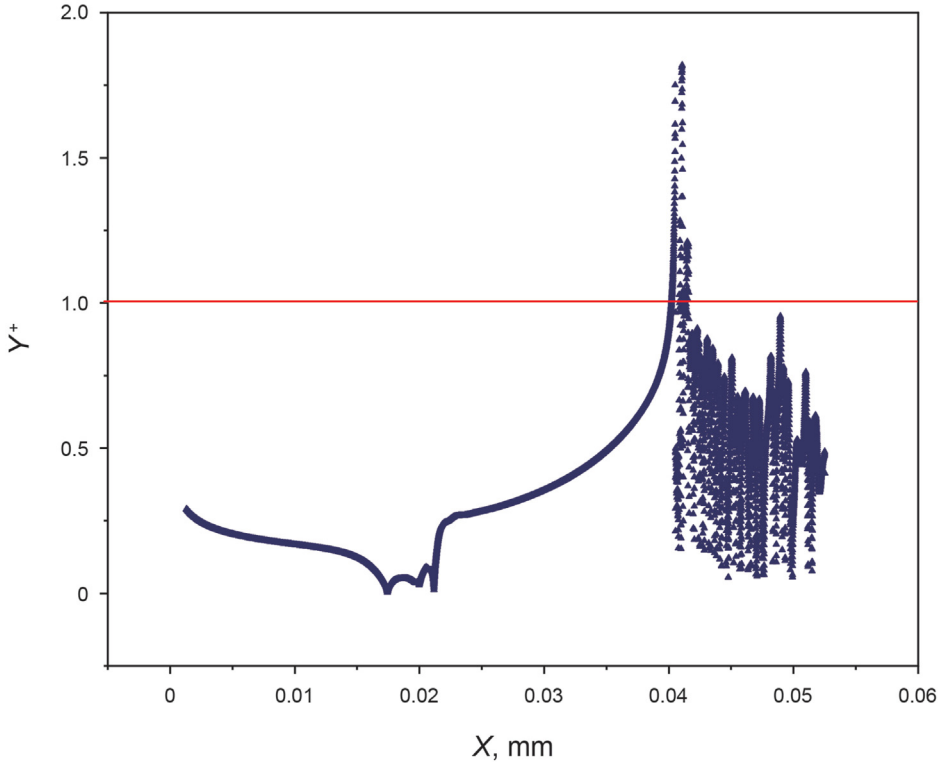

Fig. 3. Distribution of y^+ along the wall surface.

operator, also specific to the WALE model given by

$$D_w = \frac{\left(S_{ij}^d S_{ij}^d\right)^{3/2}}{\left(\bar{S}_{ij}\bar{S}_{ij}\right)^{5/2} + \left(S_{ij}^d S_{ij}^d\right)^{5/4}} \tag{10}$$

where S_{ij}^d is the traceless, symmetric part of the square of the resolved velocity gradient tensor. There are numerous sub grid-scale models available for modelling the eddy-viscosity term. The WALE model was preferred due to its proper cubic near wall behavior, omitting the need for a dynamic coefficient model which can increase computational time.

2.4. Model validation

RNG k-epsilon model is used to verify the accuracy of the LES model in this paper, and enhance wall treatment is used to obtain the more accurate flow data. The centerline velocity distribution is shown as Fig. 4, the centerline velocity shows that the simulations results of LES are in a good agreement with RNG k-epsilon model, several cross sections are chosen to analyze the difference of velocity profiles of the RNG k-epsilon model and LES simulations shown as Fig. 5. As the Fig. 5 shows, all the main flow field velocity profiles show a good agreement, there is a little difference appeared at $x = 0.02$, the velocity data of the LES simulation has a delay growth compared to the RNG k-epsilon simulation. The RNG k-epsilon model can only simulate the average flow parameters, the boundary layer transition can't be simulated accurately while the LES model can capture the small-scale vortexes when the grid is fine enough. In this paper the near wall grid is fine enough to capture the real flow state of boundary layer transition for $y^+ \approx 1$, the LES model used in this paper has the capability to simulate the real flow state inside the nozzle.

In order to verify the accuracy of the numerical model, a numerical simulation was performed on the same calculation model as J.G.M.EGGELS did, and the results were compared with its experimental data and direct simulation results (Eggels et al., 1994). As shown in Fig. 6, it shows good consistency, with a maximum error of 0.03, to prove the accuracy of the model.

3. Simulations results

In this section, three different inlet velocities are set to investigate the flow properties of internal flow of the cone-straight nozzle with the Reynolds number increasing. The inlet velocities are set to 1 m/s, 5 m/s and 10 m/s and some monitoring locations are placed as Fig. 7 shows. These points can reveal the flow properties of the converging section, the turning points and the nozzle throat. The following analysis of simulation results are based on the chosen points.

3.1. Velocity distribution

The velocity distributions of the monitoring locations are shown as Fig. 7 the velocity distribution profiles are shown as Fig. 8 there is some interesting performance, the center velocity is greater than the velocity near the wall at $x = 0.017$ m, and the flow state remains same until the end of the converging section (also named as the entrance of the throat), at $x = 0.04$ m, the flow state shows a big difference with the front, the velocity near the nozzle wall is greater than the centerline velocity. And the gradient of the velocity distribution near wall is sharper. There is a delay of the velocity growing at $x = 0.02$ m, which is the first turning point of the nozzle and the entrance of the converging section. At $x = 0.045$, the velocity profile shows the same trend with the monitoring points placed at the converging section.

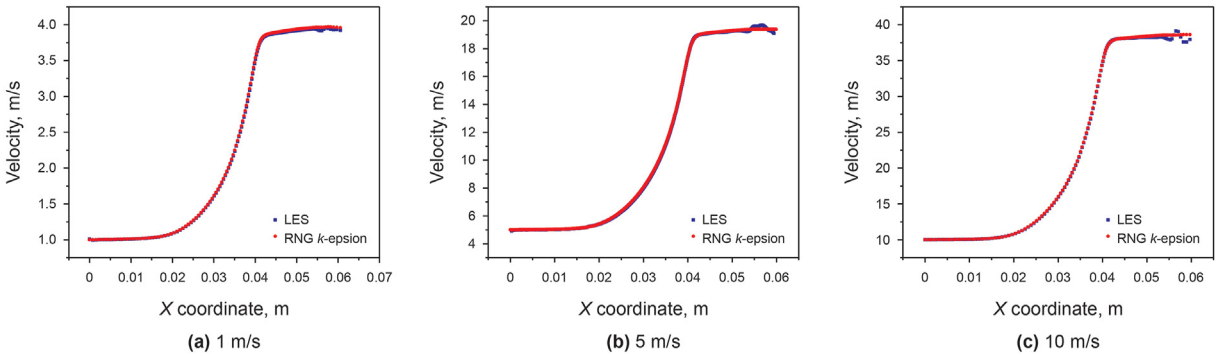

Fig. 4. Comparison of centerline velocity of LES model and RNG k-epsilon.

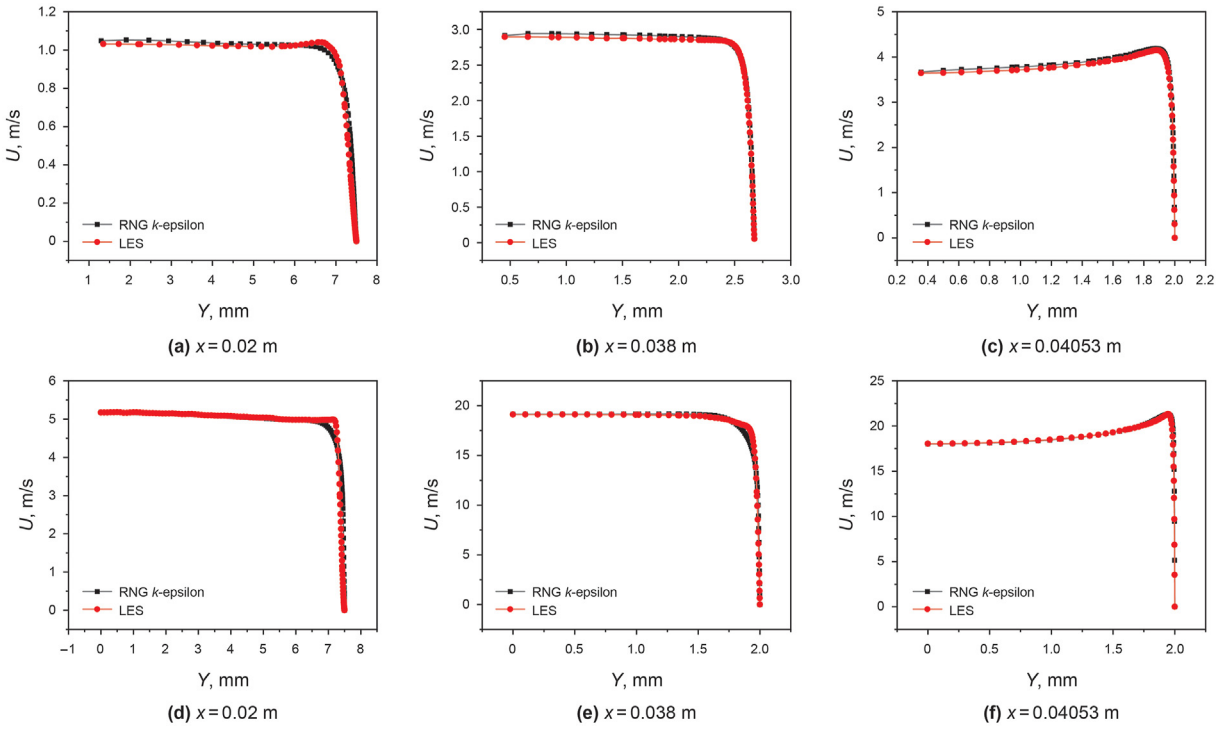

Fig. 5. Comparison of radial velocity of LES model and RNG k-epsilon model.

The internal flow velocity contour is shown as Fig. 9, the main flow fields of the three cases show the similar performance, while there is a difference shown at the near wall flow, there are a series of vortex rings appearing near the wall when the inlet velocity is set to 5 m/s and 10 m/s, and the phenomenon doesn't appear when the inlet velocity is 1 m/s the vortex rings appear intermittently, the distance between the rings is not consistent. The velocity peak appears in the end of the converging section, the velocity distribution of the main flow field in the throat section shows the similarity.

3.2. Boundary layer thickness

The boundary layer thickness is theoretically the distance from the position corresponding to 99% of the central main field velocity to the wall, and the thickness decreases with the velocity growing, however, due to the lower velocity and the instability, the profile of the boundary layer is difficult to distinguish. So, the distance between the position where the velocity corresponding the 90% is defined as the boundary layer thickness in this paper. To obtain the profile of the boundary layer, many monitoring locations are set as the Fig. 10 shows.

And three different simulation results with different inlet velocities are depicted in Fig. 11, three curves show the similar trend along the flow direction. The rate of thickness reduction gradually decreases along the flow direction, the minimum value appears at the second turning point (the entrance of throat section). And then the thickness increases in the throat section, the growing rate decreases along the flow direction.

3.3. Dynamic pressure

Dynamic pressure is the difference between total pressure and static pressure, which can characterize the situation of irregular movement to some extent. Fig. 12 shows the wall dynamic pressure of the three simulations with different inlet velocity along the flow direction. As the pictures show, the dynamic pressure increases slowly in the converging section and achieved a peak value at the

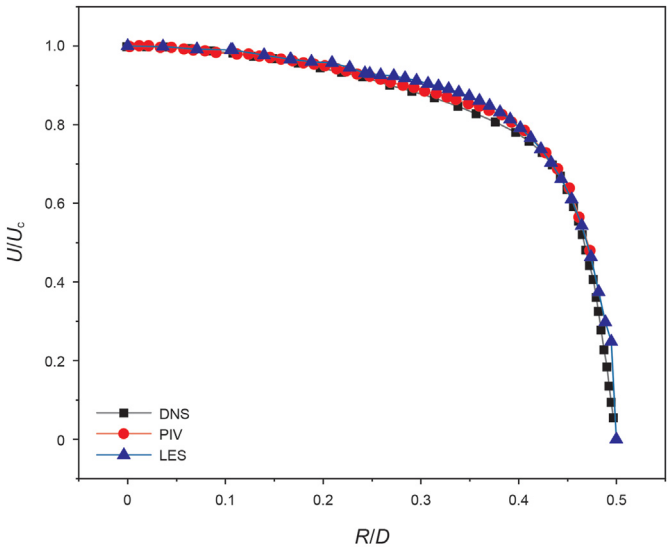

Fig. 6. Comparison among LES, DNS and experimental data.

end of the converging section with a sharp peak, the three cases show the same similar trend in the converging section. The peak value decreases sharply and then remains close to 0 when the inlet velocity is set to 1 m/s while there is a big difference between the other cases with inlet velocity set to 5 m/s and 10 m/s there is a fluctuation appearing in the throat section, the fluctuation when the inlet velocity is set to 5 m/s is more regular than when the inlet velocity is set to 10 m/s and the dynamic pressure in throat section increases with the inlet velocity.

3.4. Wall shear stress

Viscous shear stress along the nozzle wall is shown as the Fig. 13, the mean shear stress profile is the same as the instant shear stress at the lowest inlet velocity, the shear stress increases in the converging section and decreases sharply at entrance of the throat section, then gradually becomes stable. The other two mean wall shear stress profiles show the same trend. While the other two instant wall shear stress show a difference with a fluctuation as the dynamic pressure profile does.

3.5. Skin friction coefficient and turbulence intensity

Flow resistance mainly includes friction resistance and kinetic energy dissipation, the former mainly occurs in the boundary layer, and the latter is mainly caused by irregular movement. The skin friction coefficient along the nozzle wall is depicted in Fig. 14. The mean skin friction coefficient and instant skin friction both show the same trend as the wall shear stress and won't be described again here.

Root mean square error (RMSE) of the velocity is utilized to evaluate the turbulence intensity, the RMSE velocity is shown as Fig. 15. At $x = 0.017$ m, there is a peak value of RMSE velocity appears near the wall when the inlet velocity is set to 10 m/s, and then small fluctuations appear along the radial line. There are no obvious peaks appear in the flow field when inlet velocity is set to 1 m/s the value of RMSE velocity remains stable along the nozzle wall, there is a little increase appearing near wall even though at the turning point. When the inlet velocity increases to 5 m/s, there is small fluctuations filling the whole flow field, and the fluctuations become increasing severe especially in the field near the wall, there appears a peak value when the fluid arriving at the throat section.

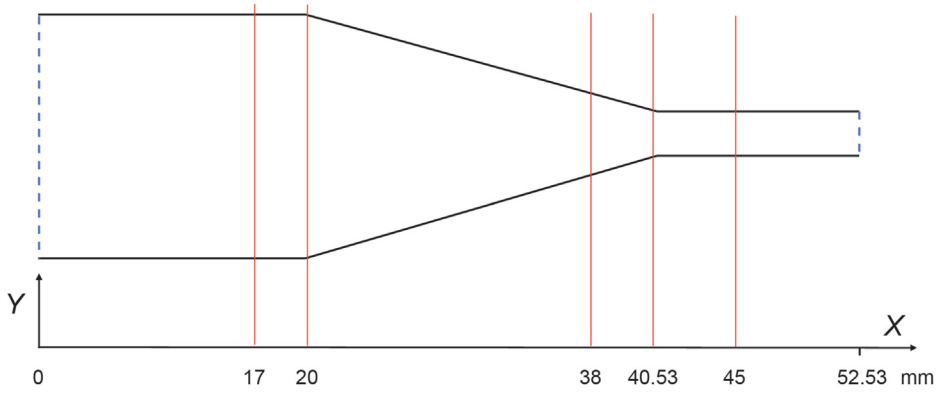

Fig. 7. Monitoring locations.

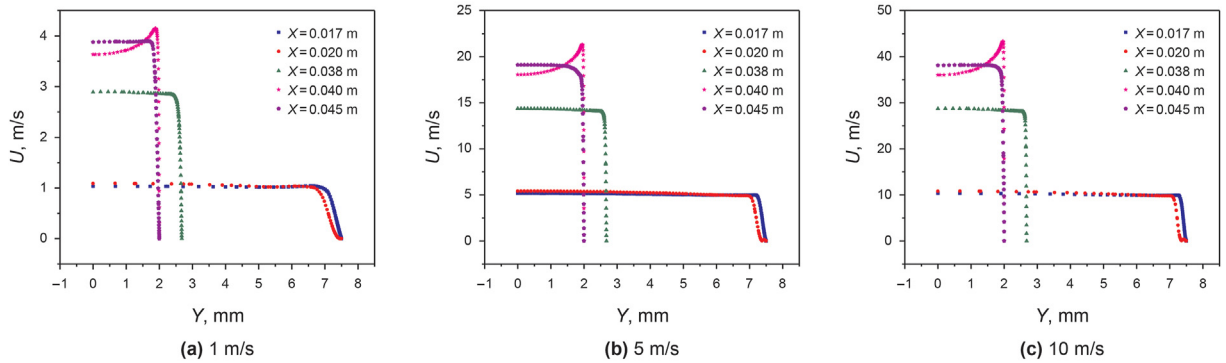

Fig. 8. Velocity distribution at different location.

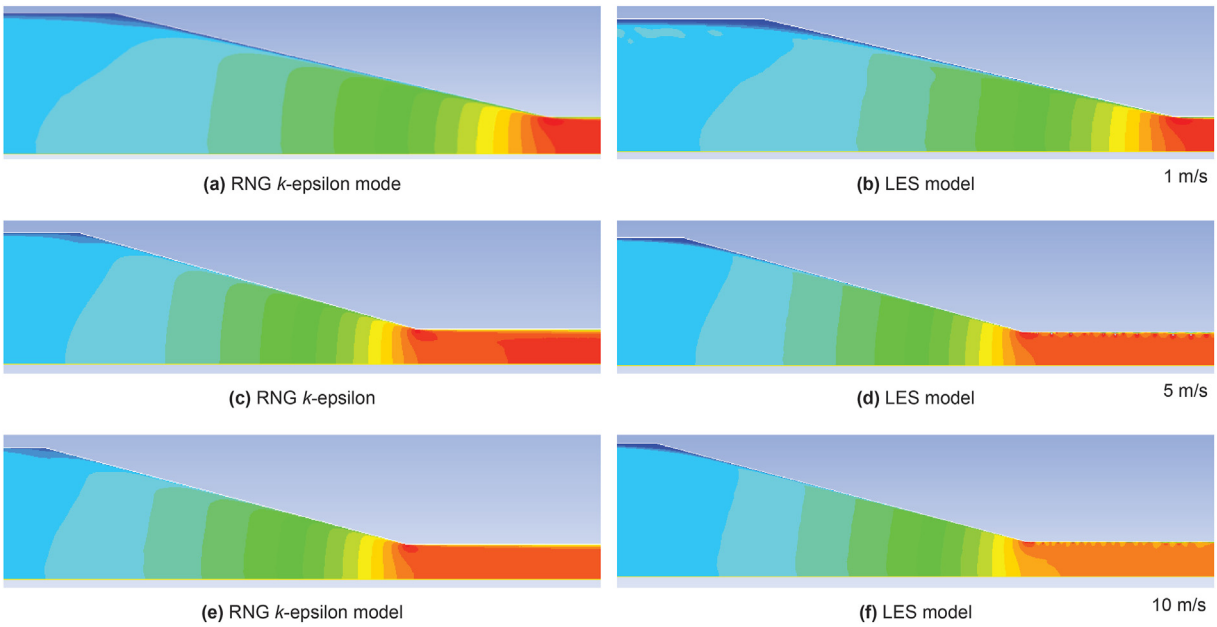

Fig. 9. Contours of velocity distribution at different inlet velocities.

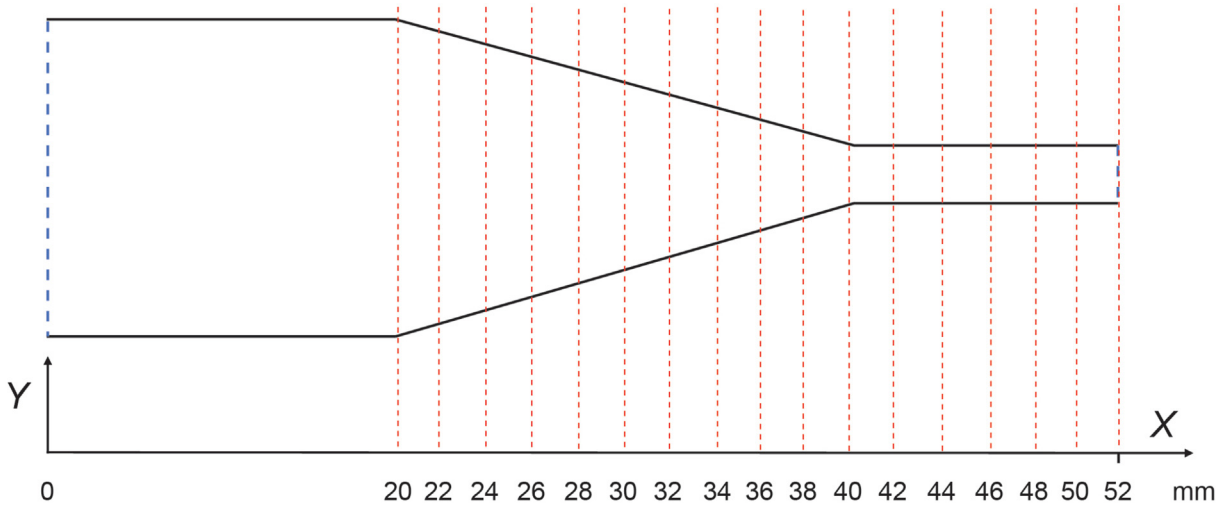

Fig. 10. Monitoring locations.

When the inlet velocity is set to 10 m/s, fluctuations appear in all flow field, and the peak value appears near wall throughout the flow, the fluctuation intensity is more severe than the other two.

3.6. Reynolds stress

The stresses are unique to turbulence and are caused by the pulsation of fluid particles, called Reynolds shear stress including normal stress ($u'u'$ and $v'v'$) and tangential stress ($u'v'$). Reynolds stress can be used to analyze the flow pulsion. The Reynold stress curves are shown as Figs. 16 and 17. When the inlet velocity is set to 1 m/s, at $x = 0.017$ m and 0.02 m, the Reynolds stress value in the main flow field is nearly zero, the pear value appeared near the wall, and then the fluid flows through the converging section the normal stress begins to fluctuate until the fluid flow into the throat section, at $x = 0.04$ m, the Reynolds stress is expressed as the overall maximum, the Reynolds stress in the main low field gradually becomes stable and closes to a number.

While there are fluctuations thought all the flow zoon when the inlet velocity is set to 5 m/s, the normal stress peak appears near the wall at $x = 0.02$ m where is the entrance of the converging section, and then the fluid flows thought out the converging section with increasing normal stress and more fluctuations, the higher normal stress peak appears when the fluid arriving at the turning point, when the fluid flow into the throat section, the peak value comes to the largest value as 2500 Pa.

4. Discussions

4.1. Boundary layer velocity distributions

The LES model has the capacity to capture the small-scale flow properties, the boundary layer velocity distributions are shown as the Fig. 18, at $x = 0.017$ m, the velocity profiles of the cases with inlet velocity of 5 m/s and 10 m/s show similar trend and the max value of U^+ is closed, the flow state of main field is thought to be a

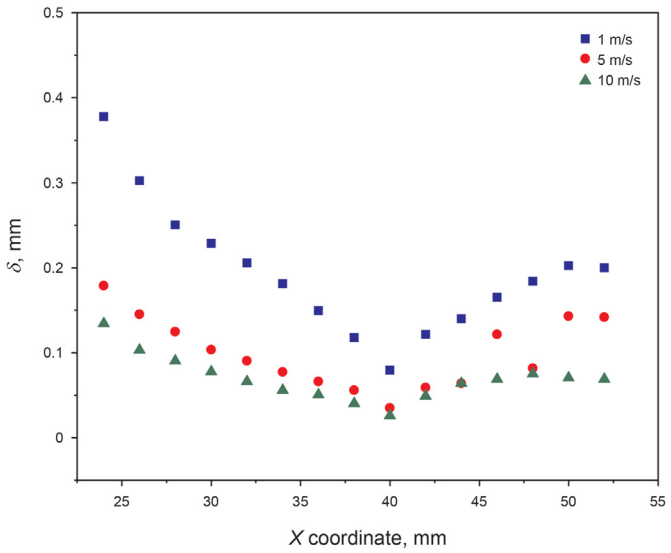

Fig. 11. Boundary layer thickness at different inlet velocities.

turbulent flow. The case with inlet velocity of 1 m/s with lower U^+ and larger boundary layer thickness is thought to be a laminar flow. And the viscous bottom layer, logarithmic rate layer and buffer layer can be distinguished clearly.

At $x = 0.02$ m, the velocity profile shows a difference with that at $x = 0.017$ m, there is a delay in velocity growth when the inlet velocity is set to 5 m/s and 10 m/s, as the Fig. 19 shows, there is an eddy appearing at this place due to the excitation of the converging slope, the fluid particles with high speed form a backflow when impacting on the slope. The backflow particles exchange momentum with the inlet flow particles and lost some kinetic energy, so the flow field around the backflow eddy shows a smaller speed as the picture shows, and the outer flow forms new viscous bottom layer, logarithmic rate layer and buffer layer. The turbulence is too weak to form a backflow when the inlet velocity is 1 m/s, so the boundary layer velocity profile shows the same as that at $x = 0.017$ m.

At $x = 0.038$ m, 0.04 m (turning point) and 0.045 m, the three velocity distribution profiles show the same trend, when the fluid particles are accelerated in the converging section, the boundary layer will be compressed, so the viscous bottom layer is too thin to be distinguished as well as in throat section. There is an interesting phenomenon appearing at $x = 0.04$ m where is the entrance of throat section, the centerline flow velocity is lower than that near the wall, there is an angle between the direction of fluid flow and the direction of the centerline of the throat. The momentum conversion will occur when the fluid particles near wall meet at this location, and the central fluid particles will lose kinetic energy and show a lower velocity. And this interesting phenomenon disappears when flowing into the throat section due to the weaker exchange of momentum of the meeting.

So, the meeting of fluid particles appeared at the turning point resulting in the irregular movement, that is why the pear value of the dynamic pressure and wall shear stress appearing at this point. The boundary layer is compressed when the fluid flowing through the converging section, more and more fluid particles impact on the slope, the irregular movement becomes more and more severe, the turbulence intensity increases along the converging direction, the boundary layer is most compressed at the turning point, the irregular movement of particles evolves most at the turning point, so the boundary layer thickness is thinnest, the wall shear stress and the dynamic pressure grow along the converging direction and reach the maximum value at the turning point ($x = 0.04$ m).

Reynolds stress represents the intensity of velocity fluctuation, which is related to the flow turbulence intensity. Boundary layer is the place where the momentum exchange occurs, so the turbulence intensity increases from zero in this place. The turbulence intensity will decrease outside the boundary layer if the flow state is laminar and will close to or fluctuate around a specific value when the flow state is turbulent. Reynolds stress perform the same way. In converging section, the turbulence intensity increases along the converging direction due to the increasingly irregular movement, and Reynolds stress and turbulence intensity have an overall increasing trend in converging section. In throat section, turbulence intensity and Reynolds stress will fluctuate around a specific value in main flow field when turbulent flow is restricted and becomes relatively stable.

4.2. Boundary layer transition and separation

Boundary layer transition occurs when encountering an excitation, and boundary layer separation occurs when backpressure gradient appears. For cone-straight nozzle, the excitation appears at the entrance of converging section and throat section, and the separation only occurs at the entrance of throat section. As the velocity contours show, boundary layer transition does appear at the two points and typical vortex structures are found in these two points, boundary layer separation does occur at the entrance of throat section, and the alternating appearance of eddy laminar flow proves this as the velocity contours show. The boundary layer transition occurred at the entrance of converging section dose not survive in the following journey with the low inlet velocity and the slope restriction. While the boundary layer transition and separation occur at the same point and the velocity is higher, so the vortex flow survived and appears alternately. The dynamic pressure and

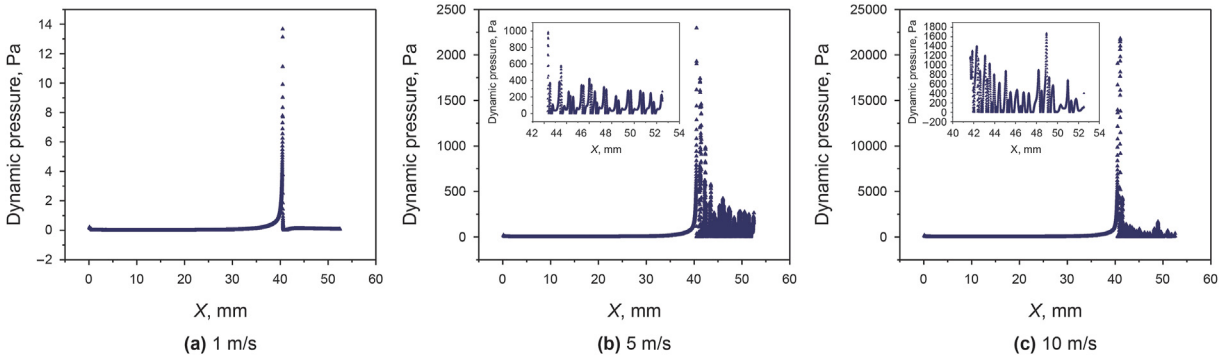

Fig. 12. Dynamic pressure at different inlet velocities.

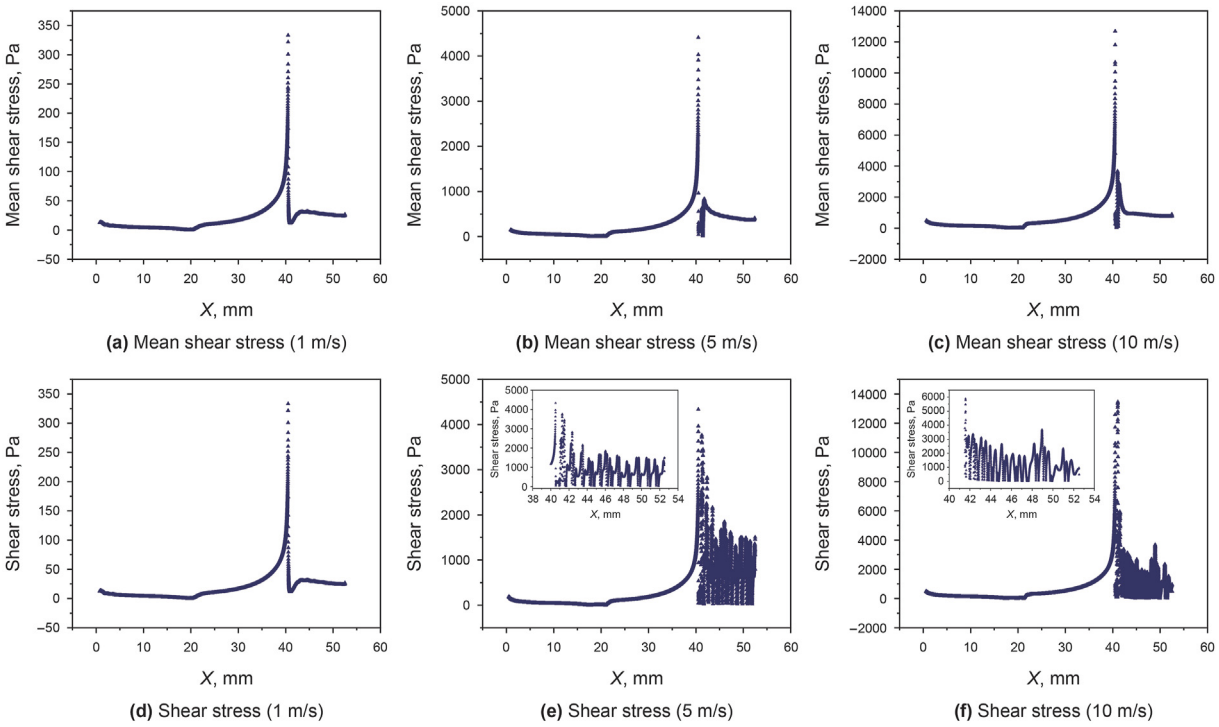

Fig. 13. Mean and instant wall shear stress at different inlet velocities.

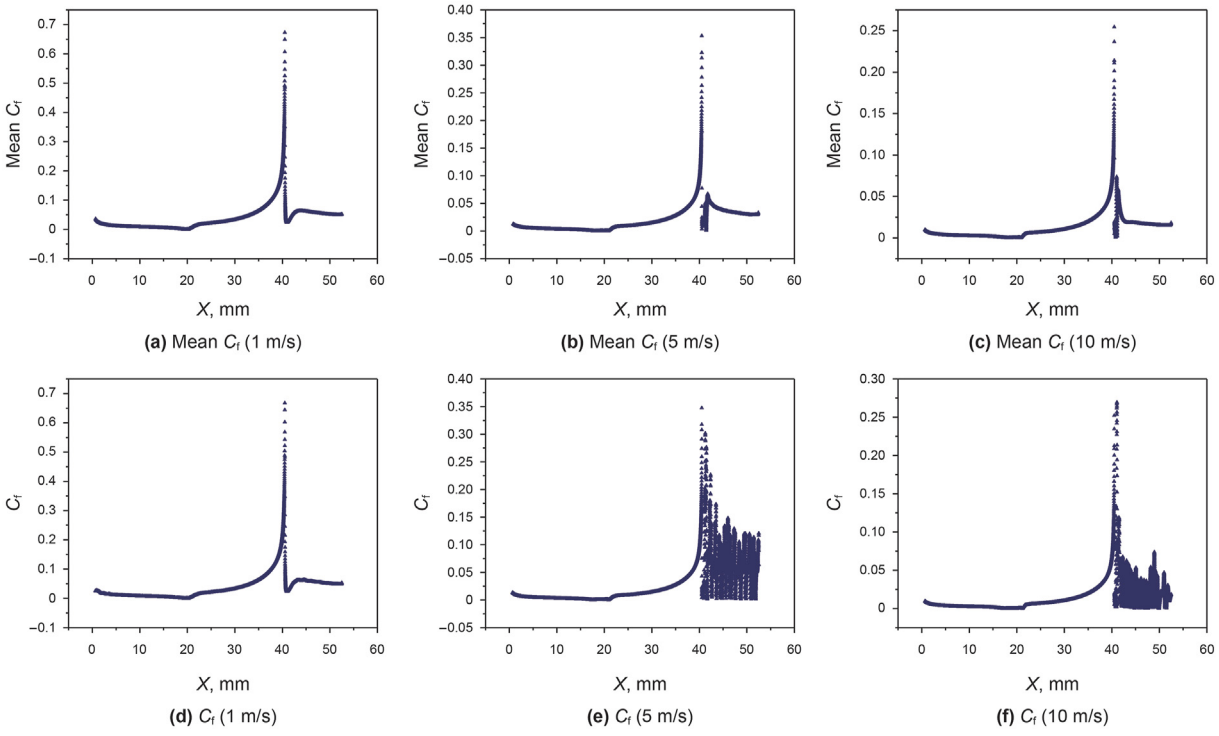

Fig. 14. Mean and instant skin friction coefficient at different inlet velocities.

wall shear stress exhibit regular oscillations due to the eddy flow and laminar flow appearing alternately.

Boundary layer transition will cause a lot of momentum exchange and energy loss, it is necessary to suppress the occurrence of boundary layer transition when considering improving energy conversion rate and environmental protection. According to the research content of this paper, the main place where the cone-straight nozzle transition occurs is at the entrance of the throat. When considering the suppression of the boundary layer transition, it is necessary to optimize the design of the outline here. These works will be reflected in future work.

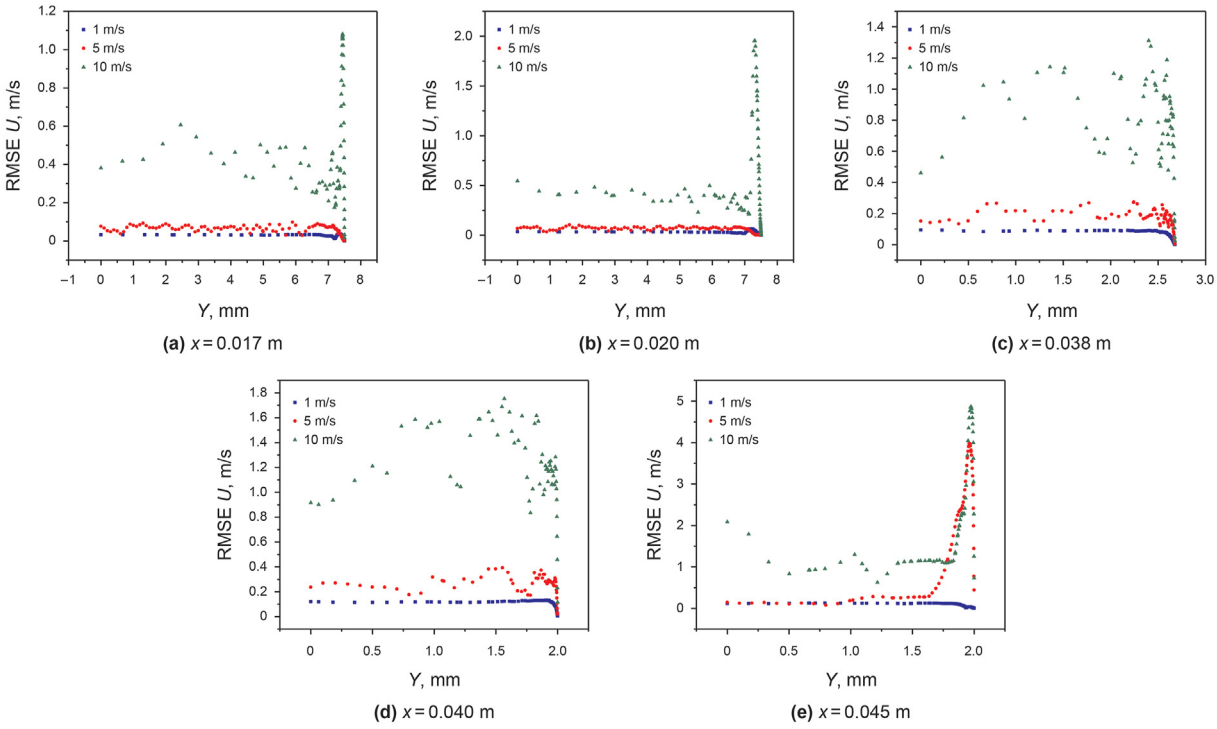

Fig. 15. RMSE velocity profile in different locations.

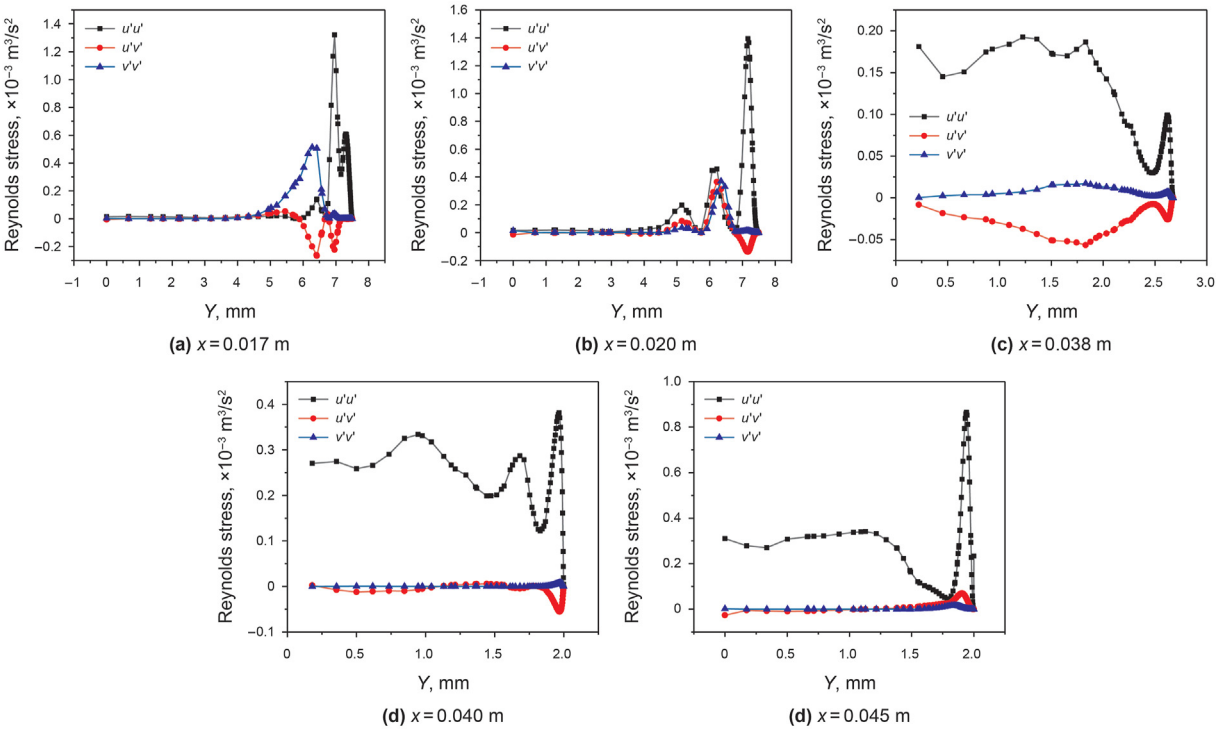

Fig. 16. Reynolds stress in different locations (1 m/s).

5. Conclusions

The LES model and RNG k-epsilon model are used in this paper to simulate the flow inside the cone-straight nozzle, LES model is validated by RNG k-epsilon model to some extent, and Emily L. Manchester validated the model by experiments. Many flow properties are analyzed. Some conclusions are drawn as follows.

The flow state of the boundary layer near wall of the nozzle is basically maintained as laminar flow except at the entrance and end of the converging section when the inlet velocity is low like 1 m/s as simulated. And the state of throat section changes to turbulent, and the laminar flow and vortex flow appears alternately

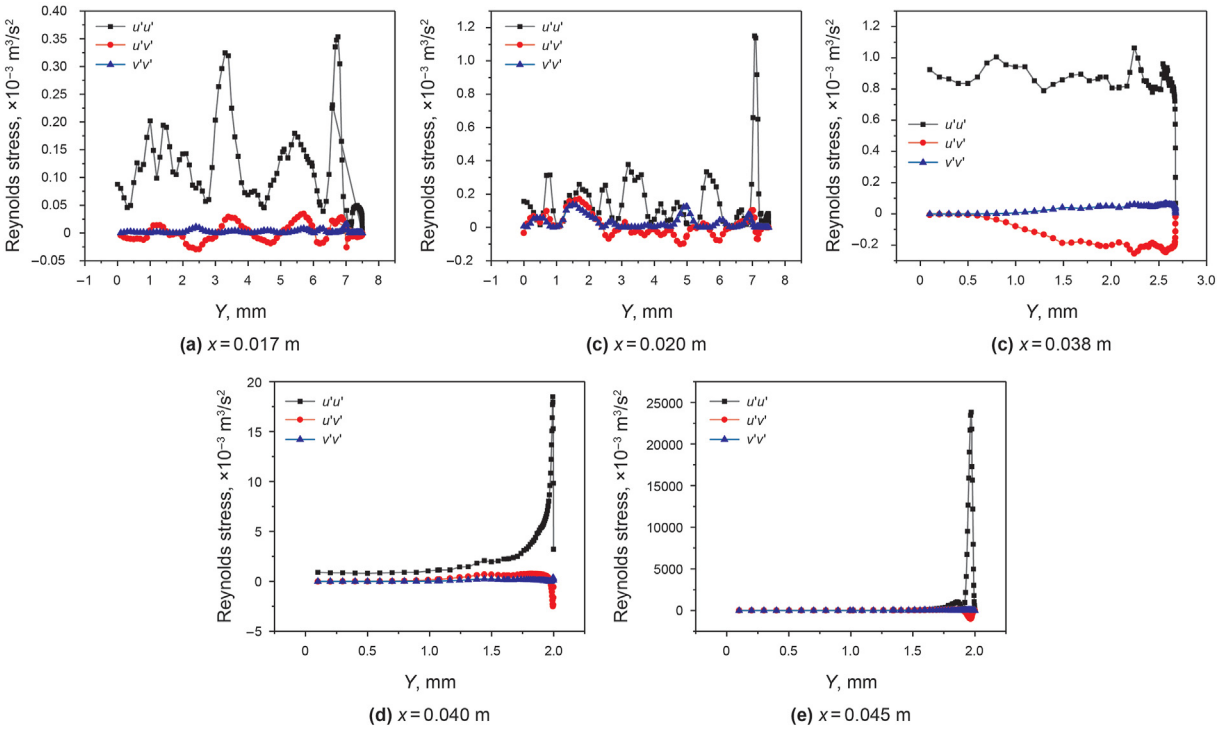

Fig. 17. Reynolds stress in different locations (5 m/s).

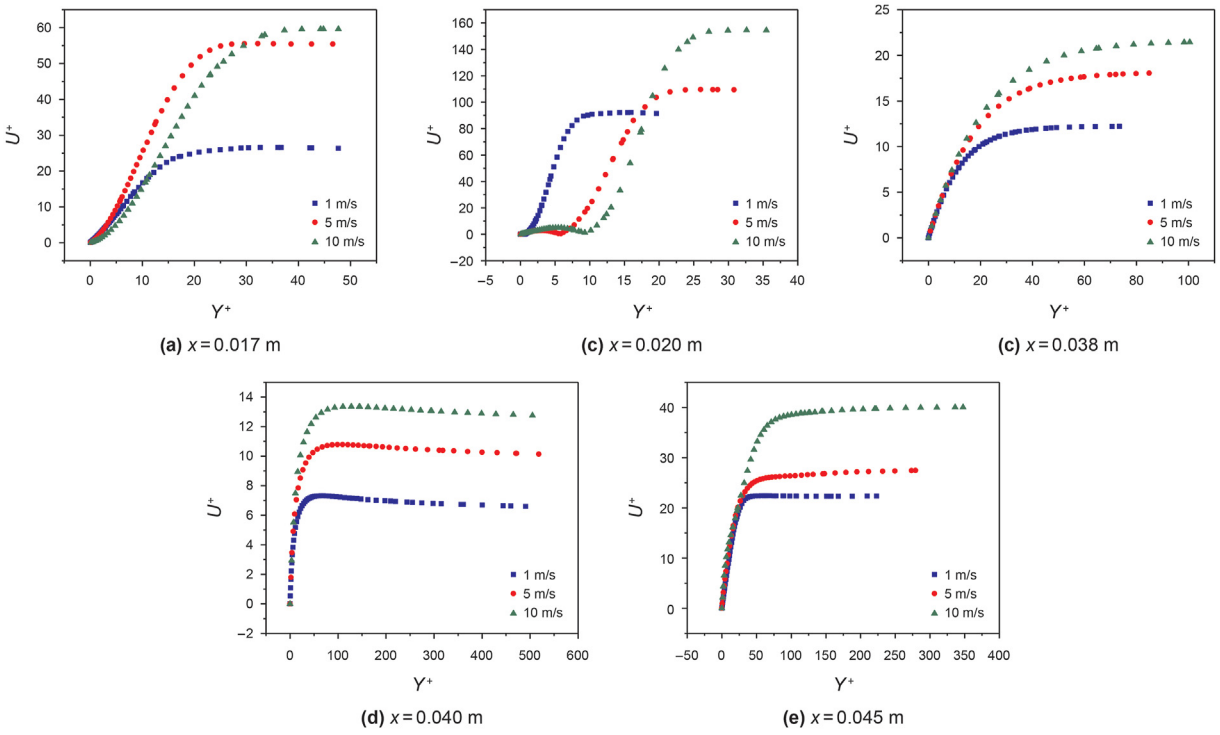

Fig. 18. Boundary layer velocity distribution in different locations.

in the throat section like when the velocity is set to 5 m/s as simulated. There is a critical conversion value here need to be investigated in the future. Boundary layer separation occurs at the entrance of throat section due to the backpressure gradient, the transition occurs at the entrance of the converging section and throat section, the vortex can be distinguished. And a typical vortex sequence structure appears in throat section and is thought to be the result of the combined effect of boundary layer transition and separation when the inlet velocity is set higher than the critical velocity.

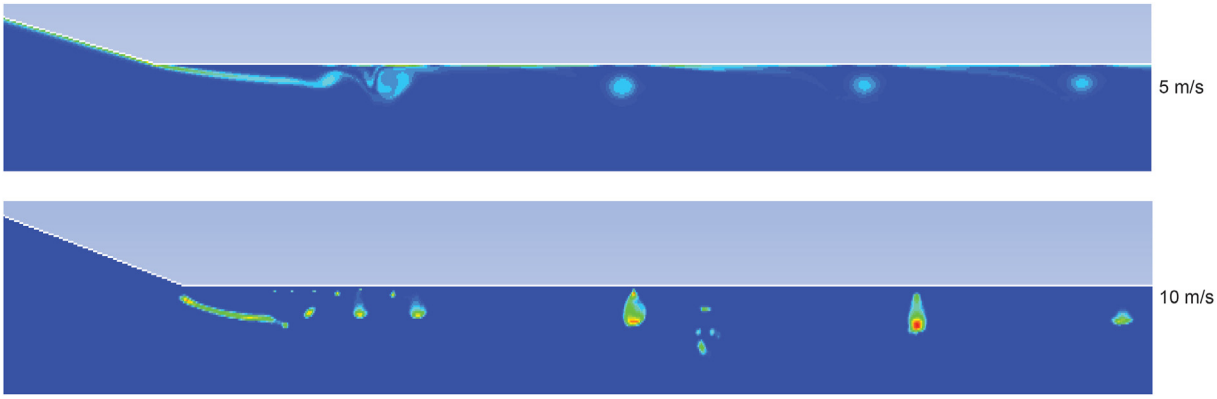

Fig. 19. Vortex contours at different inlet velocities.

The fluid particles are accelerated in the converging section, the velocity is high in center and low near the wall initially, and gradually are transferred to high near the wall and low in the center, the reason is that fluid particles with velocities in different directions gradually meet, and the collision suppresses the development of the central velocity. The most severe meeting appears at the turning point where is the area with the strongest turbulence. All these results show the same trend with dynamic pressure, wall shear stress and skin friction coefficient.

Skin friction mainly occurs near the wall, and most of the friction resistance occurs in the throat section due to the turbulent state of the boundary layer. The transition outline from the converging section to the throat section needs to be optimized when considering reducing the flow resistance.

Above all, the main flow resistance occurs in throat section, longer flow core length and higher discharge coefficient are main factor considered in drilling and wellbore cleaning. To obtain an optimized cone-straight nozzle, the transition from the converging section to the throat section requires optimized design, it is necessary to reduce the length of the throat as much as possible while meeting the clustering capacity. All the work is to increase the rock breaking effect, save hydraulic energy and improve the energy conversion efficiency when the cone-straight nozzle is used in petroleum drilling.

Declaration of competing interest

The authors declare no conflict of interest.

Acknowledgements

The authors would like to thank the financial support from National Key Research and Development Program of China (2019YFB1504202), 111 Plan (Grant No. B17045) and the National Science Fund for Distinguished Young Scholars (Grant No. 51725404).

References

Bogey, C., Bailly, C., 2010. Influence of nozzle-exit boundary-layer conditions on the flow and acoustic fields of initially laminar jets. J. Fluid Mech. 663, 507–538. https://doi:10.1017/s0022112010003605.

Brès, G.A., Jordan, P., Jaunet, V., Le Rallic, M., Cavalieri, A.V.G., Towne, A., Lele, S.K., Colonius, T., Schmidt, O.T., 2018. Importance of the nozzle-exit boundary-layer state in subsonic turbulent jets. J. Fluid Mech. 851, 83–124. https://doi.org/10.1017/jfm.2018.476.

Chen, T., Liao, W., Li, X., Jing, Z., Gong, Y., 2019. Design and optimization of jet nozzle structure based on Fluent. J. Chengdu Univ. (Nat. Sci. Ed.) 38 (3), 304–307 (**in Chinese**).

Dong, Z.Z., Guo, C., Xi, Y.Q., 2016. Simulation analysis of flow field of high-pressure water jet nozzle based on CFD[J]. Petrol. Chem. Equip. 19, 20–23 (**in Chinese**).

Eggels, J., Unger, F., Weiss, M., Westerweel, J., Adrian, R.J., Friedrich, R., Nieuwstadt, F., 1994. Fully developed turbulent pipe flow: a comparison between direct numerical simulation and experiment. J. Fluid Mech. 268, 175–210. https://doi.org/10.1017/S002211209400131X.

Folkes, J., 2009. Waterjet—an innovative tool for manufacturing. J. Mater. Process Technol. 209, 6181–6189. https://doi:10.1016/j.jmatprotec.2009.05.025.

Fontaine, R.A., Elliott, G.S., Austin, J.M., Freund, J.B., 2015. Very near-nozzle shear-layer turbulence and jet noise. J Fluid Mech 770, 27–51. https://doi:10.1017/jfm.2015.119.

Guha, A., Barron, R.M., Balachandar, R., 2011. An experimental and numerical study of water jet cleaning process. J. Mater. Process Technol. 211, 610–618. https://doi:10.1016/j.jmatprotec.2010.11.017.

Hariharan, P., Giarra, M., Reddy, V., Day, S.W., Manning, K.B., Deutsch, S., Stewart, S.F., Myers, M.R., Berman, M.R., Burgreen, G.W., 2011. Multilaboratory particle image velocimetry analysis of the FDA benchmark nozzle model to support validation of computational fluid dynamics simulations. J. Biomech. Eng. 133. https://doi.org/10.1115/1.4003440.

Ishibashi, M., 2015. Discharge coefficient equation for critical-flow toroidal-throat venturi nozzles covering the boundary-layer transition regime. Flow. Meas. Instrum. 44, 107–121. https://doi.org/10.1016/j.flowmeasinst.2014.11.009.

Ishibashi, M., Takamoto, M., 2000. Theoretical discharge coefficient of a critical circular-arc nozzle with laminar boundary layer and its verification by measurements using super-accurate nozzles. Flow Meas Instrum 11, 305–313. https://doi.org/10.1016/S0955-5986(00)00029-7.

Karon, A.Z., Ahuja, K.K., 2017. Reduction of jet noise by the nozzle-exit boundary layer. In: 23rd AIAA/CEAS Aeroacoustics Conference.

Kbmq, Z., 1985. Effect of initial condition on subsonic jet noise. AIAA J. 23, 1370–1373. https://doi.org/10.2514/3.9094.

Kim, J.H., Kim, H.D., Setoguchi, T., Matsuo, S., 2008. A computational study of real gas flows through a critical nozzle. Proc. Inst. Mech. Eng. C J. Mech. Eng. Sci. 223, 617–626. https://doi:10.1243/09544062jmes1109.

Liu, W., Cheng, X., 2020. Study on Optimization Simulation of High Pressure Water Jet Nozzle Based on Fluent, vol. 5. Energy and Environmental Protection (**in Chinese**). https://doi:10.19389/j.cnki.1003-0506.2020.05.003.

Ma, W., Pan, J., 2019. Numerical simulation of water jet flow field and rock breaking characteristics under different nozzle structures. Coal Mining Mach. 9 (**in Chinese**). https://doi:CNKI:SUN:MKJX.0.2019-09-006.

Manchester, E.L., Xu, X.Y., 2020. The effect of turbulence on transitional flow in the FDA's benchmark nozzle model using large-eddy simulation. Int. J. Numer. Method Biomed. Eng. 36, e3389. https://doi.org/10.1002/cnm.3389.

Nozzles V. Numerical Assessment of Discharge Coefficient and Wall Temperature Dependence of Discharge Coefficient for Critical-Flow.

Shi, H.H., Wang, T., Dong, R.L., Feng, Z.L., Peng, S.S., 2021. Numerical simulation of high-pressure pulsed water jet under different nozzle structures[J/OL], 2020; 10-14 J. Zhejiang Sci-Tech Univ. (Nat. Sci. Ed.) 1–8 (**in Chinese**).

Sou, A., Hosokawa, S., Tomiyama, A., 2007. Effects of cavitation in a nozzle on liquid jet atomization. Int. J. Heat Mass Transf. 50, 3575–3582. https://doi:10.1016/j.ijheatmasstransfer.2006.12.033.

Spotts, N.G., Guzik, S., Gao, X., 2013. A CFD analysis of compressible flow through convergent-conical nozzles. In: 49th AIAA/ASME/SAE/ASEE Joint Propulsion Conference.

Tafreshi, H.V., Pourdeyhimi, B., 2003. The effects of nozzle geometry on waterjet breakup at high Reynolds numbers. Exp. Fluids 35, 364–371.

Taylor, J.O., Good, B.C., Paterno, A.V., Hariharan, P., Deutsch, S., Malinauskas, R.A., Manning, K.B., 2016. Analysis of transitional and turbulent flow through the FDA benchmark nozzle model using laser Doppler velocimetry. Cardiovasc. Eng. Technol. 7, 191–209. https://doi:10.1007/s13239-016-0270-1.

Ünsal B, Koç E ,Ume T. Flow States of Critical-Flow Venturi Nozzles[J].

Ünsal, B., Rathore, K., Koç, E., 2016. Numerical findings on the boundary layer

transition of critical-flow venturi nozzles. In: 17th International Flow Measurement Conference, pp. 1–5.
Wang, C., Wang, X., Ding, H., 2018. Boundary layer of non-equilibrium condensing steam flow in a supersonic nozzle. Appl. Therm. Eng. 129, 389–402. https://doi:10.1016/j.applthermaleng.2017.10.015.
Wang, W.J., Jiang, Z.G., Chen, J.S., Jiang, L., Cao, B., 2013. Numerical simulation analysis of internal and external flow fields of nozzles with different structures [J]. Coal Mine Saf. 44, 162–165 (**in Chinese**).
Zaman, K., Bencic, T., Clem, M., Fagan, A., 2011. Shock-induced Boundary Layer Separation in CD Nozzles and its Impact on Jet Noise, vol. 2011. 49th AIAA Aerospace Sciences Meeting including the New Horizons Forum and Aerospace Exposition, p. 1031. https://doi.org/10.2514/6.2011-1031.
Zaman, K., 2017. Increased Jet Noise Due to a" Nominally Laminar" State of Nozzle Exit Boundary Layer. National Aeronautics and Space Administration, Glenn Research Center.
Zaman, K., 2012. Effect of initial boundary-layer state on subsonic jet noise. AIAA J. 50, 1784–1795. https://doi.org/10.2514/1.J051712.